

## RESEARCH ARTICLE

# Calibration of parameters for cardiovascular models with application to arterial growth

Sebastian Kehl | Michael W. Gee

Mechanics and High Performance Computing Group, Technische Universität München, Parkring 35 Garching bei, 85748, München

**Correspondence**

Michael Gee, Mechanics and High Performance Computing Group, Technische Universität München, Parkring 35, 85748 Garching bei München.  
Email: gee@tum.de

**Funding Information**

Deutsche Forschungsgesellschaft, Grant/Award Number: GE2254/1-1

**Abstract**

We present a computational framework for the calibration of parameters describing cardiovascular models with a focus on the application of growth of abdominal aortic aneurysms (AAA). The growth rate in this sort of pathology is considered a critical parameter in the risk management and is an essential indicator for the assessment of surveillance intervals. Parameters describing growth of AAAs are not measurable directly and need to be estimated from available data often given by medical imaging technologies. Registration procedures often applied in standard workflows of parameter identification to extract the image encoded information are a source of significant systematic error. The concept of surface currents provides means to effectively avoid this source of errors by establishing a mathematical framework to compare surface information, directly accessible from image data. By utilizing this concept it is possible to inversely estimate growth parameters using sophisticated numerical models of AAAs from measurements available as surface information. In this work we present a framework to obtain spatial distributions of parameters governing growth of arterial tissue, and we show how the use of surface currents can significantly improve the results. We further present the application to patient specific follow-up data resulting in a spatial map of volumetric growth rates enabling, for the first time, prediction of further AAA expansion.

**KEYWORDS**

abdominal aortic aneurysms, arterial growth, data assimilation, parameter identification, surface currents

## 1 | INTRODUCTION

Rupture of abdominal aortic aneurysms (AAA) causes a life-threatening risk for elderly people. For example, in the United Kingdom the overall mortality rate in case of rupture is 65% to 85% in men above 65 years of age<sup>1</sup>. Although overall mortality rates can be reduced by selective repair, it was reported that early selective repair does not necessarily save lives.<sup>2</sup> This fact raises the need for surveillance policies to safely balance the frequency of examination with the risk of rupture. The assessment of surveillance intervals poses a daily challenge for doctors, and the development of guidelines is an area of ongoing research. Thereby decision making is mostly based on measurements of the maximum aortic diameter. Statistical models trying to indicate risk factors for AAA

growth are exploited to predict changes in maximum diameter, see, eg, Brady et al.<sup>3</sup> It is clear that risk factors such as patient sex, family history, and smoking status despite showing statistical significance for the prediction of AAA growth do not model but merely describe the actual physical process. It can therefore be expected that the use of computational models incorporating these physical processes have the potential to significantly improve predictions on AAA growth. This expectation can be further substantiated by the possibility of computational models to exploit available follow-up image data (and the information encoded therein) by means of data assimilation techniques beyond solely measuring changes in diameter. As a step toward the application in clinical practice, we therefore introduce a computational framework to estimate spatial distributions of parameters describing arterial

wall growth of patient-specific AAA models from follow-up image data.

Modeling progression and degradation of human soft tissue is a challenging field and existing approaches range from purely kinematic growth models<sup>4</sup> and their application to arterial wall growth,<sup>5</sup> the incorporation of remodeling and the constrained mixture theory<sup>6</sup> to latest results addressing the issue of vascular homeostasis.<sup>7</sup> We refer to the study of Humphrey and Holzapfel<sup>8</sup> for a more comprehensive overview of growth and remodeling (G&R) in aortic tissue and aneurysms. Common to all G&R-modeling approaches is that to be used in a predictive manner a set of patient-specific parameters has to be identified. The identifiability of these parameters, and therefore also the applicability of the presented approach in clinical routine at some point, will thereby be constrained by the available data.

With respect to cardiovascular applications, these data mostly result from medical imaging techniques. With the increasing power and availability of such image data (computed tomography [CT], magnetic resonance imaging, and ultrasound), data assimilation techniques have been increasingly applied to augment the personalization of models beyond solely using patient-specific geometries. Particular progress was made in the area of sequential parameter identification<sup>9</sup> with a broad variety of applications, see, eg, Bertoglio et al.,<sup>10</sup> Chabiniok et al.,<sup>11</sup> Nagler et al.,<sup>12</sup> and Barber et al.<sup>13</sup> A similar spectrum is covered by variational approaches, see, eg, Sermesant et al.,<sup>14</sup> Perego et al.,<sup>15</sup> Zhao et al.<sup>16</sup>, Kroon and Holzapfel<sup>17</sup>, and Gokhale et al.<sup>18</sup> with most work being directed toward the estimation of elastic tissue properties. Few attention is given to the inverse estimation of G&R-parameters in a patient-specific setting. In the study of Zeinali-Davarani,<sup>19</sup> a set of parameters of a G&R-model is identified from an imaged state such that homeostatic conditions are obtained for a patient-specific aorta model subject to the loading conditions during imaging. Further growth and remodeling is then initiated from this state, and predictions are made based on the identified parameters. In contrast, we are interested in the identification of heterogeneous distributions of growth parameters of diseased patients. Therefore, we make use of follow-up data, showing at least 2 different stages of the disease, to calibrate our model. Due to the quasi-static nature of the boundary value problem, we choose to model arterial growth, cf, Section 2, and the possibility to very efficiently guide an iterative optimization algorithm by means of the adjoint equations within the variational framework, we opt for the variational setting.

Additionally we want to highlight a phenomenon specific to a special class of inverse problems based on position measurements. Results of these approaches crucially depend on how these measurements are handled. In many applications measurements are implicitly provided by medical imaging technology and are conveniently extracted from the images by the application of image registration techniques. These

techniques, being again inverse problems, rely on modeling assumptions, which are not necessarily in good agreement with the model to be fitted later. We will show how this systematic error can lead to significant deterioration of the final best-fit parameters and how it can easily be circumvented.

The outline of this paper is as follows: in Section 2 we introduce the mathematical description. Section 2.1 describes the modeling of AAA wall expansion, and in Section 2.2 we present the optimization approach for the parameter identification. The particular choice of similarity measures is explained in Section 2.3, and our choice of regularization for the inverse problem is stated in Section 2.4. Then we analyze our approach with synthetic data on an artificial AAA geometry in Section 3, before we apply it to a patient-specific case in Section 4. Conclusions are drawn in Section 5.

## 2 | MATHEMATICAL DESCRIPTION OF THE IDENTIFICATION PROBLEM

Our approach is based on the assumption that the timescale of the process of vascular growth (months to years) is orders of magnitude larger than the timescale of the dynamics of pulsatile blood flow (seconds). Resolving the accurate transient behavior of an artery during 1 heart cycle is therefore neither necessary nor reasonable. Instead, we consider the imaged end-diastolic state to be quasi-static with respect to the timescale of growth. This considerably reduces the computational cost, particularly when it comes to the solution of the inverse problem.

### 2.1 | Forward problem definition

To model growth of AAAs we choose as a basis the boundary value problem of stationary structural elasticity given by

$$\begin{aligned} \text{Div}(\mathbf{FS}) + \mathbf{b}_0 &= \mathbf{0} \text{ in } \Omega_0 \subset \mathbb{R}^3, \\ \mathbf{FS} \cdot \mathbf{N}_\Gamma &= \mathbf{t}_0 \text{ on } \Gamma_\sigma, \\ \mathbf{u} &= \mathbf{0} \text{ on } \Gamma_u, \end{aligned} \quad (1)$$

with the deformation gradient  $\mathbf{F} = \mathbf{I} + \nabla \mathbf{u}$  and the second Piola-Kirchhoff stresses  $\mathbf{S}$ .  $\mathbf{I}$  is the  $3 \times 3$  identity matrix. The displacement  $\mathbf{u}$  relates coordinates of the material reference configuration  $\mathbf{X} \in \Omega_0$  with coordinates of the deformed spatial configuration  $\mathbf{x} \in \Omega_t$  via the diffeomorphic mapping

$$\phi(\mathbf{X}) = \mathbf{x} = \mathbf{X} + \mathbf{u}. \quad (2)$$

In this contribution we consider homogeneous boundary conditions on the Dirichlet boundary  $\Gamma_u$  and a nonlinear traction load  $\mathbf{t}_0$  on the Neumann boundary  $\Gamma_\sigma$ .  $\mathbf{N}_\Gamma$  is the outward normal on  $\Gamma_\sigma$ . We assume the existence of an isotropic hyperelastic strain energy function  $\Psi$  such that  $\mathbf{S} = 2 \frac{\partial \Psi}{\partial \mathbf{C}}$ , with the right Cauchy-Green tensor  $\mathbf{C} = \mathbf{F}^T \mathbf{F}$ .

We follow the concept of the total Lagrangian description; thus, the material reference configuration  $\Omega_0$  corresponds to

an unloaded stress free configuration. The fact that we cannot construct this configuration from the available CT-data is taken into account by using a prestressing technique, where we choose the method of the modified updated Lagrangian formulation (MULF).<sup>20</sup>

Because we aim at solving Equation 1 by means of the finite element (FE) method we define the forward problem  $F$  via the weighted residual form of (1) given by

$$\int_{\Omega_0} \mathbf{v} \cdot [\text{Div}(\mathbf{FS}) + \mathbf{b}_0] \, dV + \int_{\Gamma_\sigma} \mathbf{v} \cdot [\mathbf{t}_0 - \mathbf{FS} \cdot \mathbf{N}_\Gamma] \, d\Gamma = 0, \quad (3)$$

whereby we choose according to the Galerkin method for the components  $u_i \in V$  and  $v_i \in V, i = 1, 2, 3$ , with

$$V = \{g \in H^1(\Omega_0) \mid \gamma_{\Gamma_u} g = 0\}, \quad (4)$$

where  $\gamma_{\Gamma_u}$  is the trace operator onto the Dirichlet boundary. Not considering body loads  $\mathbf{b}_0$  in the following, we can arrive at the weak form:

$$F := \int_{\Omega_0} \nabla \mathbf{v} : \mathbf{FS} \, dV - \int_{\Gamma_\sigma} \mathbf{v} \cdot \mathbf{t}_0 \, d\Gamma \quad \forall \mathbf{v} \in \{V\}^3, \quad (5)$$

with the contraction of 2-tensors  $\mathbf{G}:\mathbf{H} = G_{IJ}H_{IJ}$  using summation over repeated indices.

The volumetric growth, see, eg, Kuhl et al.,<sup>5</sup> is incorporated into this formulation by introducing the multiplicative split of the deformation gradient to

$$\mathbf{F} = \mathbf{F}_\vartheta \mathbf{F}_e. \quad (6)$$

This way, an in-between configuration  $\hat{\Omega}$  is created, where the mapping between the tangent space  $T\Omega_0$  of the material reference configuration and the tangent space  $T\hat{\Omega}$  is given by  $\mathbf{F}_\vartheta : T\Omega_0 \rightarrow T\hat{\Omega}$ . In the special case of isotropic volumetric growth  $\mathbf{F}_\vartheta$  simplifies to  $\mathbf{F}_\vartheta = \vartheta \mathbf{I}$ , where  $\vartheta$  is called the volumetric growth factor. Because the growth does not induce any stresses itself, the strain energy function is reformulated with respect to the configuration  $\hat{\Omega}$ , such that we obtain  $\hat{\mathbf{S}} = 2 \frac{\partial \Psi}{\partial \hat{\mathbf{C}}}$ . For the pull back  $\phi_*^{-1}$  of the right Cauchy-Green tensor  $\hat{\mathbf{C}}$  we have under the simplification of isovolumetric growth that  $\mathbf{C} = \phi_*^{-1} \hat{\mathbf{C}} = \vartheta^2 \hat{\mathbf{C}}$ . Similarly, for the stresses  $\mathbf{S}$  we obtain  $\mathbf{S} = \vartheta^{-2} \hat{\mathbf{S}}$ .

Because the focus of this paper is not on the modeling of arterial wall growth itself, we choose a simple evolution equation for the growth factor  $\vartheta$  of the type:

$$\dot{\vartheta} = c_\vartheta, \quad (7)$$

subject to the initial condition  $\vartheta(t = t_0) = \vartheta^0$ . Thus,  $c_\vartheta$  is the rate of change of the growth factor, and we choose it as the variable to be controlled during the optimization. Despite its simplification in accurately modeling the real physical process of growth taking place in the arterial wall, Equation 7 has 2 important advantages. On the one hand, in choosing  $c_\vartheta$  as variable to be optimized, we have a very direct control

over the result  $\vartheta$  of a possibly complicated physical growth process. This can considerably ease the numerical solution of the identification problem. On the other hand, Equation 7 is not directly in need of a homeostatic state and a “healthy” geometry as opposed to more elaborate models of arterial wall growth. Additionally, these models are usually not described by one but by a set of parameters. Given the sparsity of data in the current clinical routine, the problem of the identifiability of these parameters deteriorates as their number increases. The circumstance that healthy homeostatic geometries of the object of interest are always not available renders the identification problem increasingly uncontrollable. Taking into consideration that the methodology presented here can easily be extended to more sophisticated models, as, eg, in the study of Himpel et al.,<sup>21</sup> we think the choice of Equation 7 is a reasonable step toward applicability in a clinical context.

For the FE approximation of Equation 5, we choose a standard FE space  $V^h \subset V$ , where we use displacement based volumetric FEs. With the polynomial functions  $N_i(\mathbf{X})$  the state variable  $\mathbf{u}_e^h$  on the FE can be represented as

$$\mathbf{u}_e^h = \sum_{i=1}^n N_i(\mathbf{X}) \mathbf{d}_i, \quad (8)$$

where  $n$  is the number of nodes per element. We deploy the isoparametric concept<sup>22</sup> for the representation of the coordinates  $\mathbf{X}^h$  and  $\mathbf{x}^h$ . In this presentation we restrict the polynomial order of the  $N_i(\mathbf{X})$  to be trilinear.

For the solution of Equation 7, a simple first-order forward finite difference formula resulting in

$$\vartheta^{n+1} = c_\vartheta \Delta t + \vartheta^n \quad (9)$$

is applied, where, without loss of generality, we choose  $\vartheta^0 = 1.0$  for all the examples in this contribution.

The resulting system of nonlinear equations is solved by means of a load control scheme and a Newton-Krylov solver without step size control. Whenever necessary we switch from the Newton-Krylov solver to a more stable pseudo-transient continuation scheme.<sup>23</sup> For the solution of linear systems arising during the nonlinear iterations, we use GMRES<sup>24</sup> with AMG-preconditioning.<sup>25</sup>

## 2.2 | Lagrangian formulation of the inverse problem

The parameter identification problem is given as to find the optimal parameters  $\theta^* \in X \subset L^2(\Omega_0)$ , such that

$$\theta^* = \underset{\theta \in X}{\operatorname{argmin}} J(\mathbf{u}, \mathbf{v}, \theta), \quad (10)$$

where  $J$  is defined as the Lagrange functional

$$J(\mathbf{u}, \mathbf{v}, \theta) = D(\mathbf{u}) + \alpha R(\theta) + F(\mathbf{u}, \mathbf{v}, \theta). \quad (11)$$

Thereby we introduced the continuously differentiable functionals  $D(\mathbf{u})$  as a measure of similarity and  $R(\theta)$  as regularization on the parameter space  $X$ . For the space of parameters  $X$  we choose piece-wise constant functions, cf, Section 2.5.

For readability we omit the nonlinear dependency of the state variable  $\mathbf{u}(\theta)$  on  $\theta$  through the solution of the nonlinear forward problem  $F$ . It is this dependency that renders the solution of Equation 10 computationally demanding. To apply a gradient-based Quasi-Newton scheme (see Section 2.5), we need the Gateaux derivative  $\frac{\delta J}{\delta \theta}$  given in terms of the variation  $\delta_\theta J = \langle \frac{\delta J}{\delta \theta}, \delta \theta \rangle$ , see, eg, Grinfeld<sup>26</sup> with the Lagrange formulation, Equation 11, this can be conveniently achieved by means of the adjoint equation.

Having in mind the variation of the stresses  $\delta_\theta \mathbf{S} = \mathbb{C} : \delta_\theta \mathbf{E}$ , with the fourth-order elasticity tensor  $\mathbb{C}$  and  $\delta_\theta \mathbf{E} = \frac{1}{2}(\nabla \delta_\theta \mathbf{u}^T \mathbf{F} + \mathbf{F}^T \nabla \delta_\theta \mathbf{u})$ , see, eg, Bonet and Wood,<sup>27</sup> we can arrive at the variation  $\delta_\theta J$ :

$$\begin{aligned} \delta_\theta J = & \left\langle \frac{\delta D}{\delta_\theta \mathbf{u}}, \delta_\theta \mathbf{u} \right\rangle_{L^2(\Omega_0)} + \left\langle \alpha \frac{\delta \mathbf{R}}{\delta \theta}, \delta \theta \right\rangle_{L^2(\Omega_0)} \\ & + \left\langle \nabla \mathbf{v} : \left[ \frac{\partial \mathbf{F}}{\partial \theta} \mathbf{S} + \mathbf{F} \frac{\partial \mathbf{S}}{\partial \theta} \right], \delta \theta \right\rangle_{L^2(\Omega_0)} \\ & + \int_{\Omega_0} \nabla \mathbf{v} : [\nabla \delta_\theta \mathbf{u} \mathbf{S} + \mathbf{F}(\mathbb{C} : \delta_\theta \mathbf{E})] \, dV \\ & - \int_{\Gamma_\sigma} \mathbf{v} \cdot \frac{\partial \mathbf{t}_0}{\partial \mathbf{u}} \delta_\theta \mathbf{u} \, d\Gamma, \quad \forall \delta \theta \in L^2. \end{aligned} \quad (12)$$

Therein “:” denotes the contraction of a 4-tensor  $\mathbb{A}$  with a 2-tensor  $\mathbf{B}$ , viz.  $(\mathbb{A} : \mathbf{B})_{kl} = \mathbb{A}_{ijkl} B_{ij}$ . To circumvent the complex computation of the variation of the displacements  $\delta_\theta \mathbf{u} = \frac{\partial \mathbf{u}}{\partial \theta} \delta \theta$ , we solve the adjoint system:

$$\begin{aligned} & \left\langle \frac{\delta D}{\delta_\theta \mathbf{u}}, \delta_\theta \mathbf{u} \right\rangle_{L^2(\Omega_0)} + \int_{\Omega_0} \nabla \mathbf{v} : [\nabla \delta_\theta \mathbf{u} \mathbf{S} + \mathbf{F}(\mathbb{C} : \delta_\theta \mathbf{E})] \, dV \\ & - \int_{\Gamma_\sigma} \mathbf{v} \cdot \frac{\partial \mathbf{t}_0}{\partial \mathbf{u}} \delta_\theta \mathbf{u} \, d\Gamma = 0, \end{aligned} \quad (13)$$

for the test functions  $\mathbf{v} \in (V)^3$  such that Equation 12 simplifies to

$$\delta_\theta J = \left\langle \alpha \frac{\delta \mathbf{R}}{\delta \theta}, \delta \theta \right\rangle_{L^2(\Omega_0)} + \left\langle \nabla \mathbf{v} : \left[ \frac{\partial \mathbf{F}}{\partial \theta} \mathbf{S} + \mathbf{F} \frac{\partial \mathbf{S}}{\partial \theta} \right], \delta \theta \right\rangle_{L^2(\Omega_0)}. \quad (14)$$

This is a well-known approach with a broad range of applications.

### 2.3 | Similarity measure

The assessment of the validity of the identified parameters, ie, the quality of the description of the underlying physical process, is a question of ongoing research. Among others, this can only be tackled by considering the approximation quality of the applied model, its computational solution and the presence and proper treatment of the noise and uncertainty occurring in the data the identification process is based on. An additional problem, rarely mentioned, is the presence of systematic errors in the measurement data. This is of particular importance in cardiovascular applications, where measurements are often provided by image data, which must be processed to be applicable in data assimilation. In a

variety of applications this processing step is performed by image registration techniques, which provide displacement or strain information. This information is then often compared as reference data in a pointwise least-square sense with the displacement/strain results of the simulation model to be fitted. The influence of modeling assumptions and regularization strategies used within the image registration due to its ill-posed character is often not considered in the discussion on the quality of the fit. But the significant dependence of the final best-fit material parameters on the application of different image registration techniques in a data assimilation framework for elastic parameters of cerebral aneurysms was already shown in the study of Balocco.<sup>28</sup>

For the application presented here, we additionally have to cope with the problem that the available image data, although from the same modality, is not well suited for image registration. Due to the potentially large-time lag of several months or years between imaged states, the morphology being imaged might have changed drastically, rendering standard image registration a grand challenge. This issue could be overcome by performing the registration on a processed set of images, in the sense of a segmentation. But due to the loss of information during segmentation it is to be expected that the influence of regularization within the image registration becomes even more pronounced.

These issues can both be addressed by a sensible choice of similarity measure  $D$  in Equation 11. A very popular approach is to use the signed distance of points to surface meshes. In the context of sequential parameter identification, this concept was introduced in the study of Moireau et al.<sup>9</sup> and applied, for instance, in the study of Moireau et al.<sup>29</sup> for the identification of boundary support parameters and in the study of Bertoglio et al.<sup>10</sup> for the identification of hemodynamical parameters of a patient-specific descending aorta. Because surface data can be extracted from medical images without the application of image registration, this approach has the advantage of not being influenced by this source of systematic errors. But the signed distance surface measure can suffer from the non-uniqueness or the irrelevance of the projection point.<sup>30</sup> The concept of surface currents<sup>31</sup> was therefore applied in the context of a data assimilation framework in the study of Imperiale et al.<sup>30</sup> Therein, it is reported to effectively ameliorate the disadvantages of the signed distance measure and to improve the system observability. This is achieved by relaxing pointwise correspondences between structures and defining a measure based on global geometric similarity.<sup>32</sup> This concept was introduced for the case of surfaces in the work of Vaillant and Glaunes<sup>31</sup> with the application of surface matching and has for instance been applied in the creation of anatomical atlases.<sup>32,33</sup>

In Section 2.3.1 we therefore concentrate on the incorporation of a measure based on surface currents, which we will briefly introduce, following the works of Vaillant and Glaunes<sup>31</sup> and Durrleman et al.,<sup>32</sup> into our inverse analysis framework. To demonstrate the above-mentioned effect



of systematic errors in measurements from image registration and to show how these errors can effectively be removed from the parameter identification process, we introduce other measures incorporating registration measurements in Section 2.3.2.

### 2.3.1 | Similarity measure based on surface currents

Given an oriented surface  $\mathbb{S}$  with normals  $\mathbf{n}$ , a surface current  $S \in W^*$  is generally defined as the surface integral:

$$S = \int_{\mathbb{S}} \mathbf{w} \cdot \mathbf{n} \, d\Gamma, \quad (15)$$

thus being a linear functional on the space of test functions  $\mathbf{w} \in W$ . Given a representer  $K_{\mathbf{n}} \in W$  of  $S$ , according to the Riesz representation theorem we have that

$$\|S\|_{W^*} = \|K_{\mathbf{n}}\|_W. \quad (16)$$

To compute this norm we notice that a current can be seen as the dense span of evaluation functionals:

$$\delta_{\mathbf{n}}^x = \mathbf{w}(x) \cdot \mathbf{n}(x). \quad (17)$$

Choosing the space  $W$  to be a (vector valued) reproducing kernel Hilbert space (rkhs), with matrix kernel  $K = k(x, y)\mathbf{I}$ ,  $x, y \in \mathbb{R}^3$  and  $k : \mathbb{R}^3 \times \mathbb{R}^3 \rightarrow \mathbb{R}$ , such that

$$\forall \mathbf{c} \in \mathbb{R}^3, \quad K_x \mathbf{c} = K(x, y)\mathbf{c} \in W \quad \forall y, \quad (18)$$

we have the so-called reproducing property

$$\langle K_x \mathbf{c}, h \rangle = h(x) \cdot \mathbf{c} \quad \forall h \in W. \quad (19)$$

Comparing Equations 17 to 19 we can see that

$$\delta_{\mathbf{n}}^x = \langle K_x \mathbf{n}_x, \mathbf{w} \rangle_W = \mathbf{w}(x) \cdot \mathbf{n}(x), \quad (20)$$

and thus,  $K_x \mathbf{n}_x$  is the dual space representation of the evaluation functional Equation 17. Using Equation 16 we can therefore write

$$\begin{aligned} \langle S, S \rangle_{W^*} &= \left\langle \sum_k \delta_{\mathbf{n}_k}^{x_k}, \sum_j \delta_{\mathbf{n}_j}^{x_j} \right\rangle_{W^*} = \sum_{kj} \left\langle \delta_{\mathbf{n}_k}^{x_k}, \delta_{\mathbf{n}_j}^{x_j} \right\rangle_{W^*} \\ &= \sum_{kj} \langle K_{x_k} \mathbf{n}_{x_k}, K_{x_j} \mathbf{n}_{x_j} \rangle_W = \sum_{kj} \mathbf{n}_{x_k} \cdot k(x_k, x_j) \mathbf{n}_{x_j}. \end{aligned} \quad (21)$$

Throughout this presentation we choose  $k(x, y) = \exp(-\|x - y\|^2/\sigma^2)$ , with “kernel width”  $\sigma = 5.0$ . This value reflects our choice of scale at which we expect the similarity between the different surfaces to occur.

By summarizing the solution of the forward problem  $F$  from Equation 5 in the nonlinear operator  $\tilde{F} : X \rightarrow V$ , such that

$$\mathbf{u} = \tilde{F}(\theta), \quad (22)$$

we can make use of the associated push-forward action  $\phi_{\mathbf{u}}^{\tilde{F}} : W^* \rightarrow W^*$  on currents<sup>31</sup> via the mapping (Equation 2). So given a surface  $S$  of the computational model in the undeformed configuration and a measurement surface  $T$ , we can now define the similarity measure:

$$D_{W^*} = \left\| \phi_{\mathbf{u}}^{\tilde{F}}(S) - T \right\|_{W^*}^2. \quad (23)$$

This norm compares measurement data in the space of surfaces, which can be segmented from image data directly. Image registration to provide measurements as displacement or strain data are not needed, and therefore, its errors are not propagated through the data assimilation framework.

### 2.3.2 | Registration based similarity measures

In many parameter identification applications although, the use of image registration is prevailing, see, eg, Perego et al.,<sup>15</sup> Sermesant et al.,<sup>14</sup> and Balocco et al.<sup>28</sup> On the one hand this might be due to the easy definition of a similarity measure based on measured displacement data. On the other hand it can be very beneficial in situations where manual segmentation of measurement surfaces is not feasible because of the amount of data. The influence on the parameter identification is then heavily influenced by how these measurements are used in the similarity measure.

Because a specific choice of registration algorithm is not of particular importance for the effects we want to show, we introduce the generic registration operator  $\tilde{R} : \hat{X} \rightarrow \hat{V}$ , such that we obtain measurements:

$$\hat{\mathbf{u}} = \tilde{R}(\hat{\theta}). \quad (24)$$

With these measurements at hand, we can define the least-square measure:

$$D_Z = \frac{1}{2} \|G_F \mathbf{u} - G_R \hat{\mathbf{u}}\|_2^2, \quad (25)$$

wherein  $G_F : (V)^3 \rightarrow Z$  and  $G_R : (\hat{V})^3 \rightarrow Z$  are linear observation operators and  $Z = \mathbb{R}^m$ , with  $m$  being the number of measurements. It is important to highlight that in many applications we have  $\hat{X} \neq X$ . This practically means that the model underlying the registration algorithm is not the same as the model of the forward problem, Equation 5. It is this systematic error that will be propagated to the fitted material parameters.

To circumvent this problem, we use, similar as for the forward problem operator, Equation 22, also the measurements  $\hat{\mathbf{u}}$  define a push-forward action  $\phi_{\hat{\mathbf{u}}}^{\tilde{R}} : W^* \rightarrow W^*$  on surfaces. Applying it to a surface  $S$  of the undeformed computational model,  $\phi_{\hat{\mathbf{u}}}^{\tilde{R}}(S)$  can be used as a measurement and can be compared against a surface subject to the deformation of the forward model. Formally this is defined as

$$D_{W^*}^{\tilde{R}} = \left\| \phi_{\hat{\mathbf{u}}}^{\tilde{R}}(S) - \phi_{\hat{\mathbf{u}}}^{\tilde{R}}(S) \right\|_{W^*}^2. \quad (26)$$

Whereas Equation 25 performs a pointwise comparison of displacements measurements, the norm Equation 26 transforms these measurements into the space of surfaces, where the computation is again performed based on Equation 21.

## 2.4 | Regularization

The nonlinear identification problem, Equation 10, belongs to a general class of ill-posed problems, in the sense that large changes in the parameters  $\theta$  might lead to only small changes in the similarity measure  $D$ , which renders the problem computationally demanding, in particular for iterative methods.<sup>34</sup> A common approach to account for this is the application of the generalized Tikhonov regularization where the non-negative regularization functional  $R$  in Equation 10 often chosen to be of the form  $R = \|\mathbf{L}\theta\|_{L^2}^2$ . The choice of  $L$  as a linear differential operator enforces some smoothness on the solutions  $\theta^*$ .

Inspired by the work of Rudin et al.<sup>35</sup> the concept of total variation (TV) noise removing was also applied as regularization of identification problems of coefficients in elliptic partial differential equations, see Chan and Tai<sup>36</sup> and references therein. Particularly in the case of discontinuous coefficients, TV-regularization has proven to be advantageous over classical Tikhonov regularization.<sup>37</sup>

From the observation that aneurysms most often occur in the cerebral arteries and in the abdominal aorta, aneurysmatic growth appears to be a localized pathology. This circumstance will then also be reflected in the parameters governing arterial growth. To be able to express this localization we expect these parameters to be prone to some sort of discontinuous spatial distribution. This expectation is then reflected in the choice of the TV-functional as regularization  $R$ . Due to the piece-wise constant space  $X$  from which we choose the parameters  $\theta$ , cf, Section 2.5, we make use of a graph-based version<sup>38</sup> of the TV-functional. For a function  $b \in \mathbb{R}^N$  defined on the nodes of a graph this results in

$$R(b) = \|\nabla_w b\|_{1,2} = \sum_i \left( \sum_j w_{i,j} (b_j - b_i)^2 + \varepsilon^2 \right)^{1/2}, \quad (27)$$

where the small  $\varepsilon$  is introduced to keep the functional differentiable. The indices  $i, j$  label the nodes of the graph, and the  $w_{i,j}$  are weights between the nodes  $i$  and  $j$ , cf, Section 2.5.

## 2.5 | Numerical solution of the inverse problem

To arrive at explicitly computable formulas to evaluate Equation 14, we let  $X$  be spanned by a basis  $\{g_k(x)\}$  such that  $\theta$  can be expressed as a linear combination:

$$\theta = \sum_k^{N_{\text{ele}}} \beta_k g_k(x), \quad (28)$$

where the functions  $g_k(x)$  are defined as

$$g_k(x) = \begin{cases} 1 & \text{if } x \in \Omega_{e_k}, \\ 0 & \text{otherwise,} \end{cases} \quad (29)$$

with the volume  $\Omega_{e_k}$  defined by the FE  $e_k$  of the discretization and the total number of elements  $N_{\text{ele}}$ . With this definition, the nodes of the graph for the computation of Equation 27

are the FEs, and the connectivity of the graph is defined via the element's faces. To avoid local variations of the effective weight of the regularization  $\alpha$  due to variations in element size, the symmetric weights  $w_{i,j} = w_{j,i}$  are defined as

$$w_{i,j} = \frac{\hat{a}}{a_{i,j}}, \quad (30)$$

whereby  $a_{i,j}$  is the area of the face dividing element  $i$  from element  $j$  and  $\hat{a} = \frac{1}{N_f} \sum_k^{N_f} a_k$  with  $N_f$  being the number of all internal faces. Using such an “element-wise” distribution of parameters, in combination with the regularization, Equation 27, has the great advantage that although we might expect some sort of patchwise distribution of the final best-fit parameter distribution we do not have to a priori decide on a particular location, size, or shape of these patches.

For the computation of the current based similarity measure we follow the work by Vaillant and Glaunes<sup>31</sup> and perform a triangulation of the surfaces of the FE-mesh that we want to represent as currents. By approximation of a triangles current by the dirac currents, Equation 17, the sums in Equation 21 turn out to be sums over all the element centers of the triangulation. The distance  $d = \|S - T\|_{W^*}^2$  between a surface  $S$  and a surface  $T$  can then be computed according to

$$d \approx \sum_{fg} k(\mathbf{c}_g, \mathbf{c}_f) \mathbf{n}_f \cdot \mathbf{n}_g - 2 \sum_{fq} k(\mathbf{c}_q, \mathbf{c}_f) \mathbf{n}_f \cdot \mathbf{n}_q + \sum_{qh} k(\mathbf{c}_q, \mathbf{c}_h) \mathbf{n}_q \cdot \mathbf{n}_h, \quad (31)$$

with a triangle's normal  $\mathbf{n}$  and center  $\mathbf{c}$  and the indices  $\{f, g\}$  and  $\{q, h\}$  labeling the triangles representing the surfaces  $S$  and  $T$ , respectively.

After solving the adjoint equation, Equation 13, based on the same spatial approximation  $V^h$  as the solution of the forward problem  $F$ , we are now able to extract from Equation 14 the gradient  $\frac{\delta J}{\delta \beta_i}$  as

$$\frac{\delta J}{\delta \beta_i} = \alpha \frac{\partial R}{\partial \beta_i} + \langle \nabla \mathbf{v} : \left[ \frac{\partial \mathbf{F}}{\partial \theta} \mathbf{S} + \mathbf{F} \frac{\partial \mathbf{S}}{\partial \theta} \right], \frac{\partial \theta}{\partial \beta_i} \rangle_{L^2(\Omega_0)}. \quad (32)$$

We use this gradient within a limited memory Broyden-Fletcher-Goldfarb-Shanno (BFGS) quasi-Newton method,<sup>39</sup> with a line search strategy based on polynomial approximations<sup>40</sup> of  $J$ .

## 3 | ANALYSIS ON SYNTHETIC DATA

Before the application of the presented framework to real data, we want to analyze it using synthetic data on a simplified artificial AAA geometry, see Figure 1. This geometry incorporates an asymmetric distribution of intraluminal thrombus (ILT) and a thin layer of 1 mm of aneurysmatic arterial wall. Its diameter in the descending aorta is 22 mm from where it enlarges to mimic a rather large aneurysm with maximum diameter of 72 mm. For the computational model we make use of the symmetry in longitudinal and lateral direction,

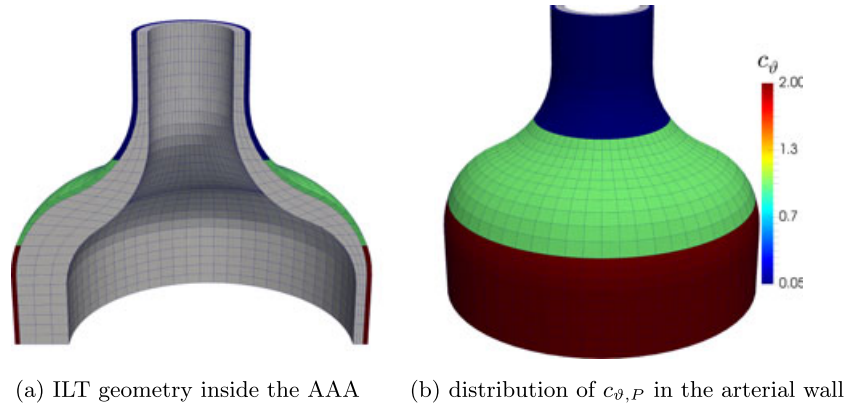


**FIGURE 1** Discretization of the synthetic abdominal aortic aneurysms (AAA) model, which utilizes symmetry in lateral and longitudinal direction. The model incorporates an asymmetric distribution of intraluminal thrombus (ILT) and a patchwise distribution of the growth parameter  $c_{\theta}$  ( $c_{\theta, p} \in \{0.05, 1.0, 2.0\}$ ) in the arterial wall

and despite not being completely physiological, we prescribe Dirichlet conditions according to Equation 1 at the proximal inlet of the aneurysm.

For the ILT we use a coupled form of the compressible neo-Hookean model<sup>41</sup> for which the strain energy function is given in terms of the first invariant  $I_1$  of the right Cauchy-Green tensor  $\hat{\mathbf{C}}$

$$\Psi_{\text{ILT}} = c_1(I_1 - 3) + \frac{c_1}{\beta_1}(\gamma^{-2\beta_1} - 1), \quad (33)$$

with  $\gamma = \det(\mathbf{F}_e)$ . For the AAA wall we use a simple but widely used model proposed in the work by Raghavan and Vorp<sup>42</sup> which, modified to near incompressibility, reads as

$$\Psi_{\text{Wall}} = \alpha(\bar{I}_1 - 3) + \beta(\bar{I}_1 - 3)^2 + \Psi_{\text{Vol}}, \quad (34)$$

where  $\bar{I}_1$  is the first invariant of the isochoric contribution of  $\hat{\mathbf{C}}$  and for the volumetric part  $\Psi_{\text{Vol}}$  we choose

$$\Psi_{\text{Vol}} = \frac{\kappa}{4}(2\ln \gamma + \gamma^2 - 1). \quad (35)$$

The parameters for these constitutive models are taken from the work of Maier et al.,<sup>43</sup> see Table 1.

For the simulation of the isovolumetric growth according to Equation 9, we define a patchwise distribution  $c_{\theta, p}$  of the parameter  $c_{\theta}$  in the arterial wall, see Figure 1B. We do not consider growth in the ILT. As a load we incrementally apply a pressure  $p = 1.0666 \cdot 10^{-2} \text{ MPa} \approx 80 \text{ mmHg}$  orthogonal to the inner surface of the synthetic aneurysm. Using the method of the modified updated lagrangian formulation<sup>20</sup> as prestressing technique we mimic diastolic conditions of a model created from real CT data. Keeping the pressure fixed we followingly simulate 1 “time step” of growth. Hence, from Equation 22

we obtain the synthetic measurements

$$\mathbf{u}^p = \tilde{F}(\theta = c_{\theta, p}), \quad (36)$$

Except for the simplification in geometry, this setup very closely resembles the approach pursued in state of the art patient-specific computational experiments. For the following analysis of the inverse parameter estimation we perform a 2-step procedure because we use the same computational mesh for the solution of Equation 36 as well as for the inverse computation. In a first step, cf, Section 3.1, we apply the data assimilation framework using Equation 23 with the measurements from Equation 36. Although blurring the solution  $\mathbf{u}^p$ , cf, Section 3.1, we cannot assess the quality of the estimation framework in a real application, because we neglect the approximation error of the spatial discretization. Whereas this question is not at the core focus of this work, we rather want to use the obtained solution from this first step to apply it as a baseline solution for the second step, cf, Section 3.2. Therein we let the measurements be generated by the application of a registration step and compare the results obtained by using the 2 different measures, Equations 25 and 26.

### 3.1 | Direct inversion of the data

For the direct inversion of the data, ie, the inverse recovery of the distribution of  $c_{\theta, p}$  shown in Figure 1B, the measurements  $\mathbf{u}^p$  from Equation 36 are blurred with white Gaussian noise (SNR = 2%) in each spatial component. Associated to these blurred measurements we can then construct measurements in the space of currents by using the push-forward action  $T^p = \varphi_*^{\tilde{F}(c_{\theta, p})}(S)$ , whereby we choose  $S$  to be the representation of the outer surface on the arterial wall. The result obtained by the application of the numerical algorithm described in Section 2.5, in combination with the current based similarity measure, Equation 23, is given in Figure 2. The weight of the regularization was set to  $\alpha = 1.0 \cdot 10^{-4}$ . It can be seen that due to the noise in the reference data the solution  $c_{\theta, D}$  can not recover the reference distribution  $c_{\theta, p}$  exactly. But

**TABLE 1** Parameters for the constitutive models, Equations 33, 34, and 35

$c_1$	18.0 kPa
$\beta_1$	4.5
$\alpha$	0.174 MPa
$\beta$	1.881 MPa
$\kappa$	104.4 MPa

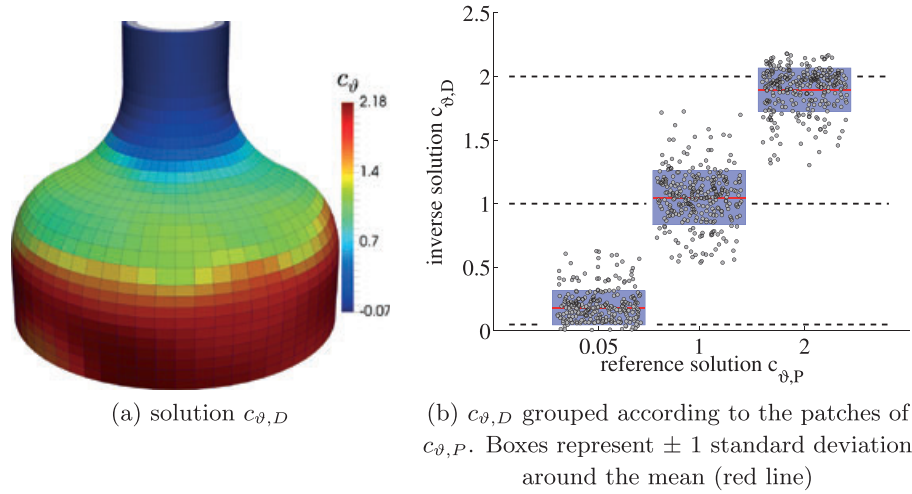


**FIGURE 2** Solution  $c_{\theta,D}$  of the direct inversion of the data subject to 2% noise. The 3 different patches of the reference solution  $c_{\theta,P}$ , as well as the mean values within these patches are well recovered<sup>†</sup>

the solution clearly shows the 3 different patches, and from Figure 2B it can furthermore be seen that the mean values within each patch are in good agreement with the reference data. The skew in the distributions of parameters in the most distal and the most proximal patch is due to the smoothing properties of the regularization. Although the TV-functional is in principle capable of representing discontinuities, in practice this property is undermined by the use of  $\varepsilon \neq 0$  to preserve differentiability of Equation 27. By the zero Neumann boundary, which is implicitly applied by Equation 27, the parameters within the top and the bottom patch are solely skewed toward the values of the inner patch, whereas for the latter the distribution remains symmetric.

Due to the “inverse crime” nature of this example we cannot infer the quality of the solution in a general setting.<sup>34</sup> But having excluded the discretization error enables us to define this solution as optimal, given the noise in the measurements. Thus, we can use it as a baseline reference to define a relative error in the following section.

### 3.2 | Registration based inversion of the data

Because the synthetic model is not based on image data, we can also not apply image registration on gray-scale images. Instead, we perform the registration step on the set of surfaces we are interested in. Namely, these are the outer surface  $S$  of the computational model and the reference surface  $T^p$  obtained from the noisy reference simulation. Therefore, we have to associate to the solution of Equation 24 an exemplary registration algorithm, cf, Section 3.2.1, which provides measurements for the parameter estimation, cf, Section 3.2.2.

#### 3.2.1 | Generating measurements using registration

Without any restriction to the effect we want to show, we choose as a framework the surface matching algorithm from Vaillant and Glaunes.<sup>31</sup> It can be summarized as follows: find the optimal solution  $v$  such that

$$J_R(v) = \hat{\alpha} \int_0^1 \|v_t\|_{\hat{V}}^2 dt + \|\varphi_*^{t=1}(S) - T^p\|_{W^*}^2, \quad (37)$$

s.t.  $\frac{\partial \varphi}{\partial t} = v(\varphi) \quad \text{on } t = [0, 1],$

is minimized. Therein  $\varphi_*^{t=1}$  represents the push-forward action on currents associated with the deformation  $\varphi$ . From the solution of Equation 37 we obtain the displacement measurements:

$$\hat{\mathbf{u}} = \varphi(t = 1). \quad (38)$$

Via the associated push-forward action, measurements in the space of currents are directly constructed as

$$\phi_*^{\hat{R}}(S) = \varphi_*^{t=1}(S). \quad (39)$$

Because a particular choice of registration algorithm is not of importance for the effect we want to show here, we refer the reader to the work of Vaillant and Glaunes<sup>31</sup> and references therein for a detailed description of the above framework and we followingly only list our choice of parameters. The spaces  $\hat{V}$  and  $W^*$  are defined via their reproducing kernels  $k(x, y) = \exp(-\|x - y\|^2/\sigma^2)$ , where for the space  $\hat{V}$  the kernel width  $\sigma = 10.0$  and for the space  $W^*$  the kernel width  $\sigma = 5.0$  are chosen. The weight of the energy functional is chosen to  $\hat{\alpha} = 1.0 \cdot 10^{-3}$  and the constraint is solved based on an explicit Euler time discretization with 5 time steps. We want to highlight that the modeling assumptions in this framework are controlled via the kernel defining  $\hat{V}$  and the weight  $\hat{\alpha}$ . It is obvious that these parameters, despite minimizing the functional in Equation 37 effectively, are not necessarily capable of representing the kinematics of some complicated arterial growth process.

<sup>†</sup>Data points are randomly scattered in horizontal direction within each group for better visualization. We used the “notboxplot” function provided by Rob Campbell, <https://github.com/raacampbell113/notBoxPlot>.



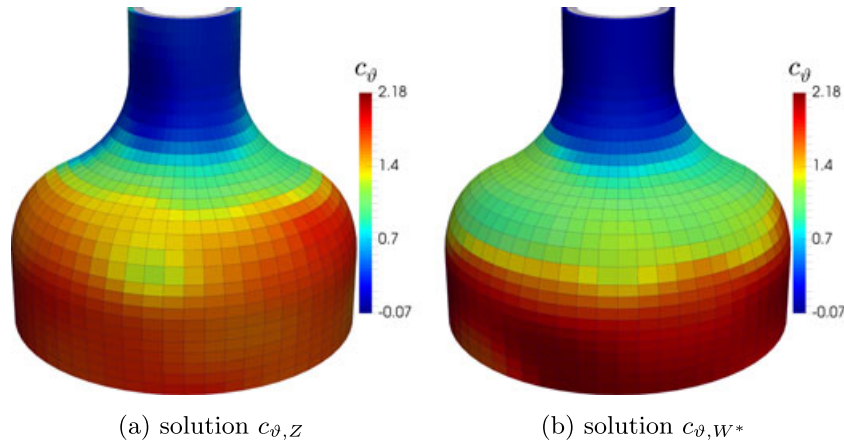


**FIGURE 3** Solutions obtained using registration measurements. (a) Result of the pointwise comparison of displacement data by application of Equation 25. (b) Result of the surface comparison in the space of currents by application of Equation 26

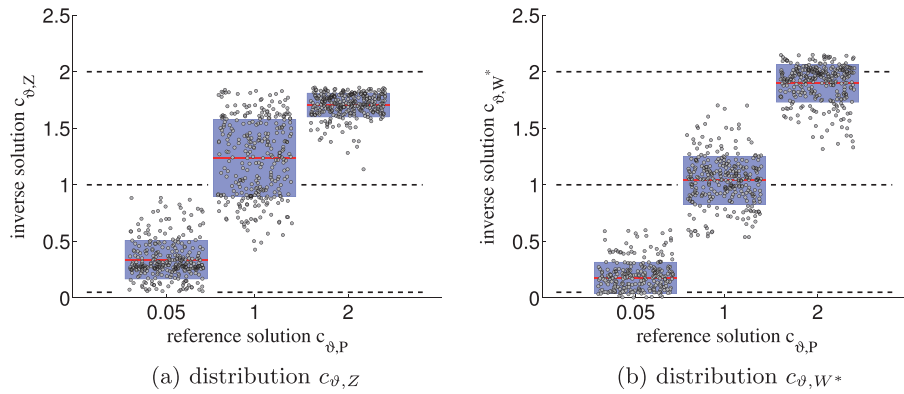


**FIGURE 4** Groupwise representation of the solutions  $c_{\vartheta,Z}$  and  $c_{\vartheta,W^*}$  of the 3 different patches of  $c_{\vartheta,P}$

### 3.2.2 | Application of registration results in the data assimilation

For the application of the measurements  $\hat{\mathbf{u}}$  from Equation 38 in the computation of the pointwise comparison, Equation 25, we consider the space  $Z$  to consist of the discrete subset of degrees of freedom of the nodes defining the model's outer surface  $S$ . The corresponding solution  $c_{\vartheta,Z}$  is given in the Figures 3A and 4A. It can be seen from Figure 3A that this solution does not recover the patches of the reference solution. This is also reflected in Figure 4A by grouping the elements according to the patches of the reference simulation and visualizing the distribution within these groups.

The solution  $c_{\vartheta,W^*}$  obtained by using the measurements  $\phi_*^{\tilde{R}}(S)$  from Equation 39 in the current based similarity measure, Equation 26, is given in Figures 3B and 4B. It can be seen that the current based similarity measure is capable to

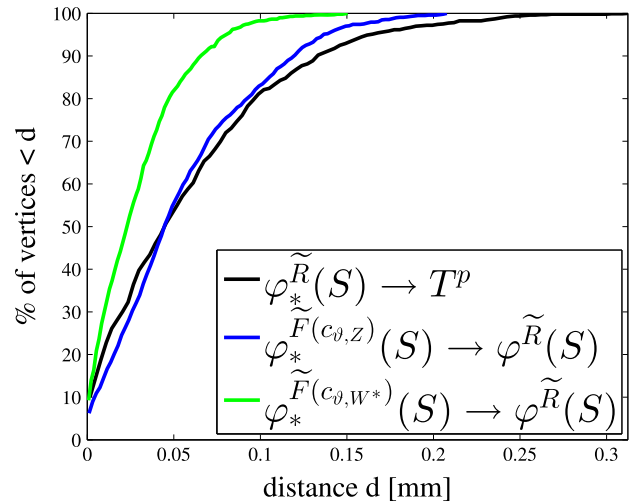


**FIGURE 5** Visualization of the quality of the fits using Equation 25 in blue and Equation 26 in green, based on the pointwise distances of the fitted model's surface to the reference surface. The distance graph of the registration is given as a reference (black). An increase in quality of the fit is indicated by steeper curves with shorter support

**TABLE 2** Relative errors  $\epsilon_Z = \|c_{\vartheta,Z} - c_{\vartheta,P}\|_2 / \epsilon_D$  and  $\epsilon_{W^*} = \|c_{\vartheta,W^*} - c_{\vartheta,P}\|_2 / \epsilon_D$  wrt. the baseline error  $\epsilon_D = \|c_{\vartheta,D} - c_{\vartheta,P}\|_2$ .

$\epsilon_Z$	$\approx 1.76$
$\epsilon_{W^*}$	$\approx 0.99$
$\epsilon_D$	$\approx 6.07$

very well recover the patchwise character of the reference solution  $c_{\vartheta,D}$ , as well as the mean values and the variances within the different patches.

For a quantification of the respective errors, we define the baseline error of the solution  $c_{\vartheta, D}$  from the direct inversion  $\epsilon_D = \|c_{\vartheta, D} - c_{\vartheta, P}\|_2$ . The relative comparison of the solutions  $c_{\vartheta, Z}$  and  $c_{\vartheta, W^*}$ , given in Table 2, shows how the current based measure outperforms the measure based on pointwise displacement data.

The difference in the quality of the 2 fits can also be analyzed in a more illustrative way from the cumulative “point to surface” distances of the vertices of the fitted surfaces  $\phi_*^{\tilde{F}(c_{\vartheta, Z})}(S)$  and  $\phi_*^{\tilde{F}(c_{\vartheta, W^*})}(S)$  to the reference surface  $\phi_*^{\tilde{R}}(S)$ , see Figure 5. It can be seen that by applying Equation 25 the measurements from the registration are matched well in the sense of the pointwise distances. But although relying on the same measurements, the application of the current based similarity measure results in a significantly closer fit. This indicates an increase in observation power of the current based similarity measure wrt. the pointwise comparison of displacement measurements.

We want to highlight that the creation of the measurements  $\hat{\mathbf{u}}$  and  $\phi_*^{\tilde{R}}(S)$  is clearly governed by an additional model, namely, the one used for the registration, which is not accounted for by the inverse parameter estimation framework. By using these measurements, we effectively avoid the inverse crime. The gain in quality of the fit by using measures in the space of currents can therefore equivalently be expected in a patient-specific example.

#### 4 | Application to patient-specific data

As a proof of concept we show the application of the presented framework to patient-specific data. A 68-year-old male patient with a relatively small AAA of  $\approx 3\text{cm}$  in maximum

diameter is considered. The generation of the patient-specific geometry is done as in the work of Maier et al.,<sup>43</sup> whereas for the mesh generation we utilize Cubit V13.2. For this patient we created an FE-mesh with 14 856 hexahedral elements, see Figure 6A. In the following we refer to this model as the computational model, which we try to fit to a reference model. The data for the latter is available through follow-up CT data, which was recorded with a time lag of 2 years. On these data we follow the same approach as for the computational model to obtain a 3-dimensional mesh geometry. To account for the change in position and rotation of the patient in the CT-scanner we prealigned the reference model to the computational model with respect to the 6 rigid body modes.

For the constitutive modeling, the application of loads and the sequence of prestressing and growth phases we choose the same setup as in Section 3. Because we cannot use any symmetry we fix the model at the most proximal inlet surface and at the 2 most distal surfaces of the 2 stubs of the iliac arteries. This choice of course will render results close to the Dirichlet boundary highly unphysiological whereas far enough we expect the effects of this boundary constraint to diminish.

As for the artificial model we are again interested in finding the volumetric growth rate  $c_{\vartheta}$  within the AAA wall such that the computational model best fits the reference model. Due to the analysis in Section 3 we want to directly define this best fit in terms of Equation 23. Because the thickness of the AAA wall cannot be detected from CT imaging, we will base the inverse analysis on surface information of the outer surface of the ILT. Therefore, we associate to the outer ILT surface of the computational model the surface  $S$  and to the outer ILT surface of the reference model the surface  $T$ , see Figure 6B. The weight of the regularization

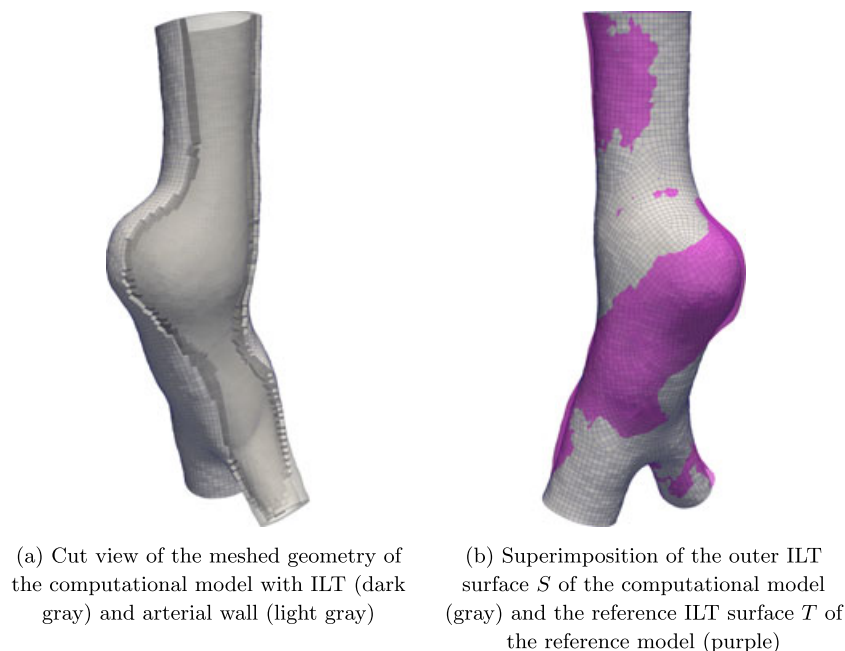
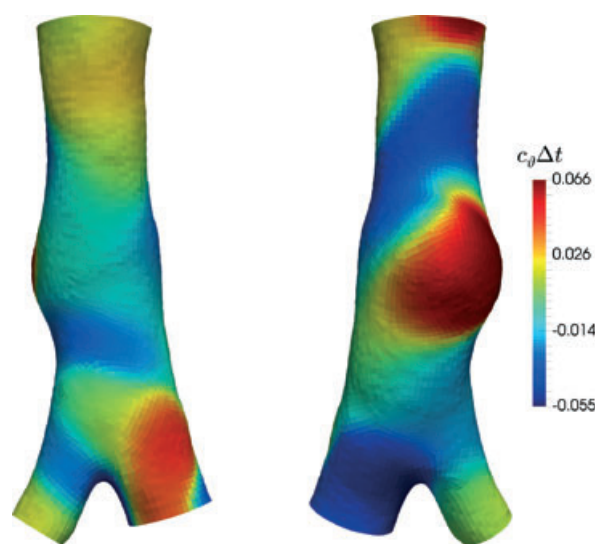


**FIGURE 6** Patient-specific abdominal aortic aneurysms data. (a) Showing mesh for the computational model and (b) surface data to be used for the parameter identification

is set to  $\alpha = 1.0 \cdot 10^{-4}$ . The best fit parameter distribution for this setup is given in Figure 7. Thereby we visualized  $c_\theta \Delta t$ , which gives a direct indication of the growth induced volumetric part of the total deformation for the time interval  $\Delta t \approx 2$  years. A distinct region of increased growth is located in the anterior part of the aneurysm sac whereas there is another distinct region of volume reduction in the posterior region.

An impression of the quality of the fit can be obtained by investigating the pointwise distances of the vertices of the outer ILT surface  $S$  of the computational model to the counterpart surface  $T$  of the reference model, see Figure 8.

An impression of the local quality of the fit can be obtained by mapping the pointwise distances to the surface  $S$ . It can be seen that the distance between  $S$  and  $T$  in the anterior



(a) posterior perspective (b) anterior perspective

**FIGURE 7** Spatial distribution of the growth induced volumetric component  $c_\theta \Delta t$  of the total deformation

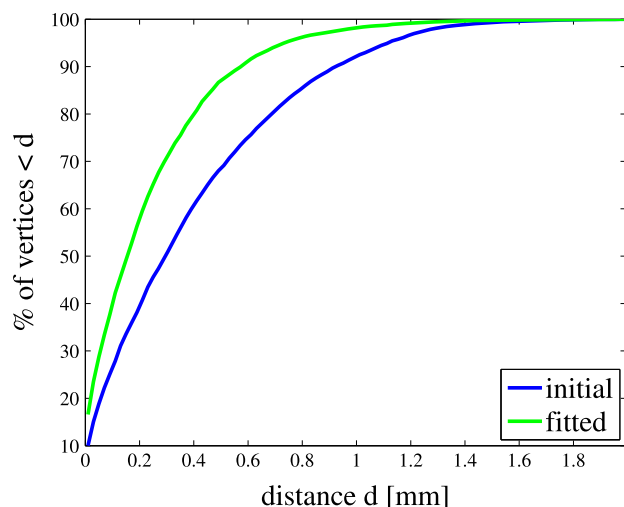


**FIGURE 8** Pointwise distance graph for model surface  $S$  to reference surface  $T$  before (blue) and after the fit (green)

area of the aneurysm sac is effectively reduced, see Figure 9, whereas in the posterior area it remains a region of increased distance, see Figure 10. It can also be seen that due to the Dirichlet conditions the distances at the boundaries remain unchanged rendering the results with respect to the growth parameters close to the boundaries physiologically meaningless. Whereas the deviations at the boundary are obviously connected to the kinematic incompatibility, the reason for the “imperfect” fit distant from the boundaries are manifold. In the first place, the similarity is evaluated at a user-defined scale of space introduced through the kernel chosen for the

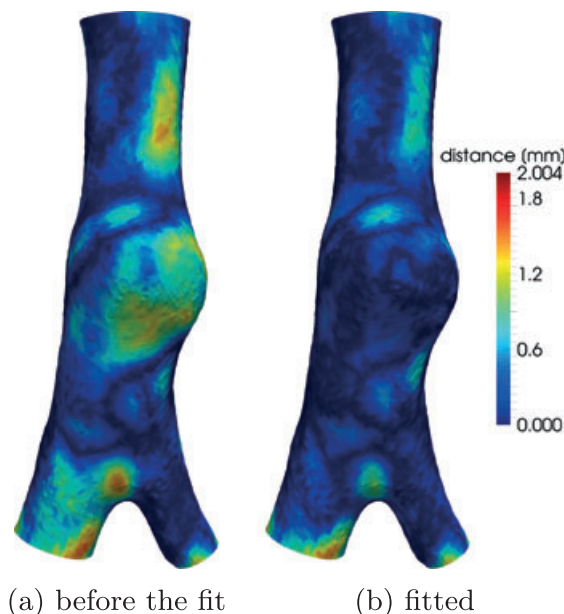


**FIGURE 9** Pointwise distance of the vertices in  $S$  of the computational model to the reference surface  $T$ . Anterior perspective

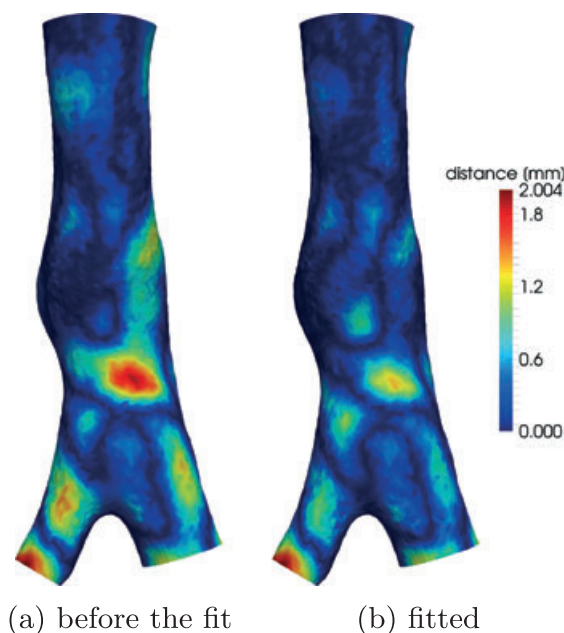


**FIGURE 10** Pointwise distance of the vertices in  $S$  of the computational model to the reference surface  $T$ . Posterior perspective

computation of Equation 21. Thus, the fit of the surfaces is smeared out and optimality is not achieved pointwise. Furthermore, the reference surface  $T$  is still subject to noise in the imaging machinery or systematic errors in the segmentation process, which might render the reference model incompatible with the underlying growth model, resulting in deviations from an “optimal” fit. Finally, it is clear that the simple model, Equation 7, might not be optimal with respect to the complex biomechanical growth processes in the arterial wall, and it is expected that the application of more sophisticated models can improve the fit quality. The same argument holds for the model deficiencies in terms of discretization size or the application of element technology.

## 5 | CONCLUSION

We presented a computational framework for the inverse estimation of growth parameters for patient-specific models based on follow-up data. We qualitatively analyzed the effect of 2 different similarity measures in the objective function of the data assimilation framework. It was shown that measuring similarity in the space of surface currents can significantly improve results with respect to similarity measures based on pointwise displacements.

For the first time, to the authors’ best knowledge, we are able to compute a spatial distribution of a patient-specific volumetric growth rate from follow-up CT data. Due to the amount of information being used in this calibration phase, we expect that modeling further growth based on the estimated parameters can significantly increase the accuracy in predictions of changes in maximum diameter. The verification of this capability is a next step toward the applicability as a tool to help in the assessment of surveillance intervals in clinical practice. This can only be achieved by the application of the proposed framework to a statistically significant cohort of data. Thereby also more complex and tortuous geometries should be considered to prove robustness of the proposed approach.

We want to highlight that the presented framework is by no means constrained to the simple growth law, Equation 7. Extension to more sophisticated approaches can be incorporated straightforward. Whereas in this work only growth of the AAA wall was considered, the proposed framework also directly allows for the incorporation of the evolution of ILT. But degeneration, accumulation, and inflammatory processes possibly happening in the ILT-layer might not be well covered by the phenomenological growth law, Equation 7. Given a proper model of the ILT-growth and the interaction between the ILT and the growth of the AAA wall, it is a next step to evolve the approach to optimize for parameters describing ILT evolution.

Beside the consideration of growth of the ILT, also model limitations in the omission of residual stresses or fluid-structure interaction represent possible extensions of the approach for future work. Thereby the amount of available

information during the identification process is highly associated to the identifiability of the parameters and the confidence in their values. Particularly with respect to the predictive capabilities, model complexity has to be balanced with the identifiability of the model parameters. With the long-term perspective of reliable applicability in a clinical setting, the estimation of levels of confidence, or bounds thereof, is an issue to be addressed in future work.

## ACKNOWLEDGEMENTS

The authors gratefully acknowledge the support through the Deutsche Forschungs Gesellschaft (DFG, German Research Foundation), project GE2254/1-1. Further, we gratefully thank Prof Dr med C. Reeps and Prof Dr med H.H. Eckstein of the department of vascular surgery, Klinikum rechts der Isar, Technische Universität München, Germany, for providing CT image data. DFG, German research foundation GE2254/1-1IACM, International association for computational mechanics

## REFERENCES

1. Scott RAP. The multicentre aneurysm screening study (mass) into the effect of abdominal aortic aneurysm screening on mortality in men: a randomised controlled trial. *The Lancet*. 2002;360(9345):1531–1539.
2. Participants TUSAT. Mortality results for randomised controlled trial of early elective surgery or ultrasonographic surveillance for small abdominal aortic aneurysms. *The Lancet*. 1998;352(9141):1649–1655.
3. Brady AR, Thompson SG, Fowkes FGR, Greenhalgh RM, Powell JT, on behalf of the UK Small Aneurysm Trial Participants. Abdominal aortic aneurysm expansion: risk factors and time intervals for surveillance. *Circulation*. 2004;110(1):16–21.
4. Rodriguez EK, Hoger A, McCulloch AD. Stress-dependent finite growth in soft elastic tissues. *J Biomech*. 1994;27(4):455–467.
5. Kuhl E, Maas R, Himpel G, Menzel A. Computational modeling of arterial wall growth. *Biomech Model Mechanobiol*. 2007;6(5):321–331.
6. Humphrey JD, Rajagopal KR. A constrained mixture model for growth and remodeling of soft tissues. *Math Models Methods Appl Sci*. 2002;12(03):407–430.
7. Cyron C, Humphrey J. Vascular homeostasis and the concept of mechanobiological stability. *Int J Eng Sci*. 2014;85:203–223.
8. Humphrey J, Holzapfel G. Mechanics, mechanobiology, and modeling of human abdominal aorta and aneurysms. *J Biomech*. 2012;45(5):805–814. Special Issue on Cardiovascular Solid Mechanics.
9. Moireau P, Chapelle D, Tallec PL. Filtering for distributed mechanical systems using position measurements: perspectives in medical imaging. *Inverse Prob*. 2009;25(3):035010.
10. Bertoglio C, Moireau P, Gerbeau JF. Sequential parameter estimation for fluidstructure problems: application to hemodynamics. *Int J Numer Method Biomed Eng*. 2012;28(4):434–455.
11. Chabiniok R, Moireau P, Lesault PF, et al. Estimation of tissue contractility from cardiac cine-mri using a biomechanical heart model. *Biomech Model Mechanobiol*. 2012;11(5):609–630.
12. Nagler A, Bertoglio C, Gee M, Wall W. *Functional Imaging and Modeling of the Heart: 7th International Conference, FIMH 2013, London, UK, June 20-22, 2013. Proceedings*, vol. 7945. Springer: Berlin, Heidelberg, 2013; 132–140. Personalization of Cardiac Fiber Orientations from Image Data Using the Unscented Kalman Filter.
13. Barber DC, Valverde I, Shi Y, Brown A, Beerbaum P, Rodney Hose D. Derivation of aortic distensibility and pulse wave velocity by image registration with a physics-based regularisation term. *Int J Numer Method Biomed Eng*. 2014;30(1):55–68.



14. Sermesant M, Moireau P, Camara O, Sainte-Marie J, Andriantsimavona R, Cimrman R, Hill DLG, Chapelle D, Razavi R. Cardiac function estimation from mri using a heart model and data assimilation: advances and difficulties. *Med Image Anal.* 2006;10(4):642–656. Special Issue on Functional Imaging and Modelling of the Heart (FIMH 2005).
15. Perego M, Veneziani A, Vergara C. A variational approach for estimating the compliance of the cardiovascular tissue: an inverse fluid-structure interaction problem. *SIAM J Sci Comput.* 2011;33(3):1181–1211.
16. Zhao X, Raghavan M, Lu J. Identifying heterogeneous anisotropic properties in cerebral aneurysms: a pointwise approach. *Biomech Model Mechanobiol.* 2011;10(2):177–189.
17. Kroon M, Holzapfel GA. Estimation of the distributions of anisotropic, elastic properties and wall stresses of saccular cerebral aneurysms by inverse analysis. *Proc Math Phys Eng.* 2008;464(2092):807–825.
18. Gokhale NH, Barbone PE, Oberai AA. Solution of the nonlinear elasticity imaging inverse problem: the compressible case. *Inverse Prob.* 2008;24(4):045010.
19. Zeinali-Davaran S, Baek S. Medical image-based simulation of abdominal aortic aneurysm growth. *Mech Res Commun.* 2012;42:107–117. Recent Advances in the Biomechanics of Growth and Remodeling.
20. Gee MW, Förster C, Wall WA. A computational strategy for prestressing patient-specific biomechanical problems under finite deformation. *Int J Numer Method Biomed Eng.* 2010;26(1):52–72.
21. Himpel G, Kuhl E, Menzel A, Steinmann P. Computational modelling of isotropic multiplicative growth. *Comp Mod Eng Sci.* 2005;8:119–134.
22. Larson MG, Bengzon F. *The Finite Element Method: Theory, Implementation, and Applications*, vol. 10. Springer Science & Business Media: New York, 2013.
23. Gee MW, Kelley CT, Lehoucq RB. Pseudo-transient continuation for nonlinear transient elasticity. *Int J Numer Method Biomed Eng.* 2009;78(10):1209–1219.
24. Saad Y, Schultz MH. GMRES: a generalized minimal residual algorithm for solving nonsymmetric linear systems. *SIAM J Sci Stat Comput.* 1986;7(3):856–869.
25. Gee M, Siefert C, Hu J, Tuminaro R, Sala M. ML 5.0 smoothed aggregation user's guide. Technical Report SAND2006-2649, Sandia National Laboratories, 2006.
26. Grinfeld M (ed.). *Mathematical Tools for Physicists* (2nd edn.) Wiley-VCH Verlag GmbH & Co. KGaA: Weinheim, 2015.
27. Bonet J, Wood RD. *Nonlinear Continuum Mechanics for Finite Element Analysis*. Cambridge University Press: New York, 1997.
28. Balocco S, Camara O, Vivas E, Sola T, Guimaraens L, van Andel HAG, Majoie CB, Pozo JM, Bijnens BH, Frangi AF. Feasibility of estimating regional mechanical properties of cerebral aneurysms in vivo. *Med Phys.* 2010;37(4):1689–1706.
29. Moireau P, Bertoglio C, Xiao N, et al. Sequential identification of boundary support parameters in a fluid-structure vascular model using patient image data. *Biomech Model Mechanobiol.* 2013;12(3):475–496.
30. Imperiale A, Routier A, Durrleman S, Moireau P. *Functional Imaging and Modeling of the Heart: 7th International Conference, FIMH 2013, London, UK, June 20–22, 2013. Proceedings*, vol. 7945. Springer: Berlin, Heidelberg, 2013; 342–351.
31. Vaillant M, Glaunes J. 2005. Surface matching via currents. In *Information Processing in Medical Imaging*, Christensen GE, Sonka M (eds), Lecture Notes in Computer Science, vol. 3565 Springer: Berlin, Heidelberg, 381–392.
32. Durrleman S, Pennec X, Trounev A, Ayache N. Statistical models of sets of curves and surfaces based on currents. *Med Image Anal.* 2009;13(5):793–808. Includes Special Section on the 12th International Conference on Medical Imaging and Computer Assisted Intervention.
33. Durrleman S, Prastawa M, Charon N, et al. Morphometry of anatomical shape complexes with dense deformations and sparse parameters. *NeuroImage.* 2014;101(0):35–49.
34. Kaipio J, Somersalo E. *Statistical and Computational Inverse Problems*, Applied Mathematical Sciences. Springer: New York, 2006.
35. Rudin LI, Osher S, Fatemi E. Nonlinear total variation based noise removal algorithms. *Physica D.* 1992;60(1–4):259–268.
36. Chan TF, Tai XC. Identification of discontinuous coefficients in elliptic problems using total variation regularization. *SIAM J Sci Stat Comp.* 2003;25(3):881–904.
37. Vogel C. *Computational Methods for Inverse Problems*. Society for Industrial and Applied Mathematics: Philadelphia, 2002.
38. Hidane M, Lézoray O, Elmoataz A. Nonlinear multilayered representation of graph-signals. *J Math Imaging Vis.* 2013;45(2):114–137.
39. Nocedal J. Updating quasi-newton matrices with limited storage. *Math Comput.* 1980;35(151):773–782.
40. Kelley CT. *Iterative Methods for Optimization*, vol. 18. Siam: Philadelphia, 1999.
41. Holzapfel GA. *Nonlinear Solid Mechanics*, vol. 24. Wiley: New York, 2000.
42. Raghavan M, Vorp DA. Toward a biomechanical tool to evaluate rupture potential of abdominal aortic aneurysm: identification of a finite strain constitutive model and evaluation of its applicability. *J Biomech.* 2000;33(4):475–482.
43. Maier A, Gee M, Reeps C, Pongratz J, Eckstein HH, Wall W. A comparison of diameter, wall stress, and rupture potential index for abdominal aortic aneurysm rupture risk prediction. *Ann Biomed Eng.* 2010;38(10):3124–3134.

**How to cite this article:** Kehl S, Gee MW. Calibration of parameters for cardiovascular models with application to arterial growth. *Int J Numer Meth Biomed Engng.* 2017;33:e2822. <https://doi.org/10.1002/cnm.2822>